frontiers | Frontiers in Physics

TYPE Original Research
PUBLISHED 09 April 2025
DOI 10.3389/fphy.2025.1557330

OPEN ACCESS

EDITED BY
Zhu Xiao,
Hunan University, China

REVIEWED BY
Lixun Li,
Air Force Engineering University, China
Kai Li,
Chinese Academy of Sciences (CAS), China

*CORRESPONDENCE
Bin Fan,
fb540623907@163.com

RECEIVED 08 January 2025
ACCEPTED 11 March 2025
PUBLISHED 09 April 2025

CITATION
Yao L, Fan B, Qin H, Xian D, Gu B, Sha H, Guan G, Liu Z, He D and Zhang L (2025) A research on low-earth-orbit signal-of-opportunity interference suppression algorithm based on adaptive signal iterative subspace projection technique. *Front. Phys.* 13:1557330. doi: 10.3389/fphy.2025.1557330

A research on low-earth-orbit signal-of-opportunity interference suppression algorithm based on adaptive signal iterative subspace projection technique

Lihao Yao[1,2], Bin Fan[3]*, Honglei Qin[2], Deyong Xian[1], Boyun Gu[4], Hai Sha[1], Gangqiang Guan[1], Zhijun Liu[1], Donghan He[1] and Liwei Zhang[1]

[1]Beijing Satellite Navigation Center, Beijing, China, [2]School of Electronics and Information Engineering, Beihang University, Beijing, China, [3]PLA Army Academy of Artillery and Air Defense, Hefei, China, [4]Beijing Institute of Technology, Beijing, China

Signal-of-Opportunity (SOP) positioning based on Low-Earth-Orbit (LEO) constellations has gradually become a research hotspot. LEO satellite SOP positioning possess strong anti-jamming capabilities due to their large quantity, wide spectral coverage, and high signal power. However, few studies have deeply investigated their anti-jamming performance, particularly regarding the most common interference type faced by ground receivers - Periodic Frequency Modulation (PFM) interference. The downlink signals of LEO satellites differ significantly from those of Global Navigation Satellite Systems (GNSS) based on Medium-Earth-Orbit (MEO) or Geostationary-Earth-Orbit (GEO) satellites, making traditional interference suppression methods inapplicable. In this paper, we utilize the generalized periodicity of PFM interference signals and the characteristics of LEO constellation signals to propose an Adaptive Signal Iterative Projection and Interference Suppression (ASIPIS) algorithm. This algorithm concentrates the energy of PFM interference, which is dispersed over a wide bandwidth, into a few frequency points, enhancing the concentration of the interference and its separation from the LEO satellite signals. This effectively reduces the overlap between LEO satellite signals and interference. The algorithm then uses subspace projection to map the interference and the desired signal into different subspaces, eliminating the interference components and thus reducing the damage to the desired signal during the interference suppression process. Simulations and experiments demonstrate that compared to conventional methods, ASIPIS effectively eliminates single/multi-component PFM interference, improves suppression performance under narrow-bandwidth/high-power conditions, and overcomes limitations of traditional PFM interference suppression approaches for single-antenna LEO signal reception. The significant performance improvement in LEO anti-jamming scenarios against PFM interference confirms the algorithm's value.

KEYWORDS

signal of Opportunity, low-earth-orbit satellite, PFM, anti-jamming, adaptive signal iterative, subspace projection

1 Introduction

With the development of the Global Navigation Satellite System (GNSS), GNSS has become an important infrastructure for a country's information construction. It provides Positioning, Navigation, and Timing (PNT) services for a wide range of applications [1–5]. However, with the deepening of GNSS applications, its own shortcomings have gradually become apparent. These drawbacks primarily include: low signal power at the ground, limited frequency points, high construction and maintenance costs, and vulnerability to malicious interference, which can lead to service unavailability, especially in times of conflict or crisis [6–8]. Overcoming and addressing these GNSS shortcomings, particularly the ability to independently provide reliable and high-precision PNT services in environments where GNSS services are unavailable, has become a key focus for future development [9, 10].

Currently, nations are actively developing resilient PNT systems to ensure that military equipment can achieve accurate positioning even when GNSS performance is degraded or denied. Notably, the U.S. Department of Defense's 2020 PNT technology development roadmap highlighted the use of Signals of Opportunity (SOP) for absolute positioning, thereby supplementing GPS functionality and enhancing its availability and robustness. SOP positioning is a technology that utilizes any detectable non-navigation signals, such as acoustic, optical, electrical, magnetic, and force-based information, for positioning purposes. Given the abundance of radio signals from various applications in space, current research primarily focuses on radio-based SOP. SOP typically includes terrestrial and space-based radio signals of opportunity. However, terrestrial SOP has limited coverage and struggles to achieve seamless global coverage in areas such as deserts, oceans, and polar regions. Space-based SOP mainly refers to signals transmitted by non-navigation/non-cooperative satellites. With the recent significant development and deployment of Low-Earth-Orbit (LEO) satellites by various countries, space-based LEO satellite SOP (LEO-SOP) has emerged as a primary space-based SOP and is increasingly being applied in navigation and positioning [11, 12]. Compared to traditional GNSS-based navigation, SOP positioning using LEO satellites mainly relies on the downlink signals from communication satellites as the radiation source for positioning ground terminals. The positioning methods include instantaneous Doppler, instantaneous Doppler combined with pseudorange, and carrier phase differential techniques [13–15]. Additionally, with the rapid development of emerging satellite constellations such as Starlink and OneWeb, the large number of LEO satellites provides abundant radiation sources for space-based SOP positioning [16]. Against this backdrop, exploring SOP positioning based on LEO constellations has become a current research hotspot. Numerous studies have introduced cases where various research teams have used LEO satellites for positioning, and the research outcomes generally achieve positioning accuracy on the order of tens of meters [17–25].

At present, there is limited research on anti-jamming technologies for positioning using LEO satellite SOP. To date, only one study has been conducted on anti-narrowband interference for Iridium satellite SOP under single-antenna reception conditions [35]. Particularly for Periodic Frequency Modulation (PFM) interference, such as Periodic Linear Frequency Modulation (PLFM) and Periodic Sinusoidal Frequency Modulation (PSFM) interference signals. Currently, there has been limited in-depth research on these types of interference both domestically and internationally. PFM interference is one of the most common types of interference faced by LEO satellites SOP positioning receivers. PFM interference signals are a typical dynamic interference pattern characterized by concentrated energy, wide bandwidth, ease of implementation, and high interference efficiency. This type of interference is highly effective and relies on mature technology, making it widely used. Such interference is typically generated by malicious jammers, radar systems, or civilian radio stations and is commonly distributed across the frequency bands used by LEO satellites SOP signals [26–28]. According to surveys, over 80% of commercially available jammers utilize PFM signals as their interference source [39]. Previous research on suppressing PFM interference has primarily focused on GNSS and similar areas, with the general approach being to utilize the differences between GNSS signals and interference in the time-frequency (TF) domain, spatial domain, or spatiotemporal domain, and to propose corresponding interference suppression methods [29, 30]. Among these, using the spatial resolution of the receiver's antenna array for spatiotemporal joint processing can effectively suppress various types of interference. However, considering the high cost and complexity of terminal hardware, this method has limited applicability. In contrast, single-antenna systems, due to their small size, low cost, and low power consumption, are widely used. Therefore, detection and suppression methods for PFM interference suitable for single-antenna receivers remain a research hotspot. Currently, the most effective method is to transform the received signal into the TF domain for interference detection. Based on the different energy distribution characteristics of the received signal and interference after transformation into the TF domain, typical TF analysis methods include Short-Time Fourier Transform (STFT) [31], Wavelet Packet Transform (WPT) [32], Wigner-Ville Distribution (WVD) [33], and Fractional Fourier Transform (FrFT) [34], among others. However, STFT cannot effectively accumulate signal energy and suffers from insufficient resolution due to the fixed window width; discrete WPT is prone to spectral aliasing and amplitude distortion; WVD and other nonlinear transforms generate cross-terms that affect the parameter estimation accuracy of multi-component interference; and the non-orthogonality of discrete FrFT distorts the desired signal, with better performance only for linear frequency modulation interference. Most importantly, while these methods offer some suppression capabilities for frequency modulation (FM) interference, due to the significant overlap between the interference and the desired signal in the TF or FrFT domains, the desired signal inevitably suffers considerable damage when the interference is eliminated. This issue is further exacerbated by recent advancements in electronics, as modern small jammers can generate interference containing multiple FM components, which increases the damage to the desired signal during interference elimination.

This type of interference suppression process can be tolerated when processing downlink GNSS signals with bandwidths generally on the order of tens of MHz. However, due to the relatively narrow downlink bandwidth of LEO satellite signals (the Iridium system has a bandwidth of 500 kHz, and the Orbcomm system only 25 kHz), the signal quality degradation caused by interference suppression can severely impact the subsequent positioning accuracy. Therefore, directly applying traditional TF analysis-based interference suppression methods to PFM interference suppression in LEO satellite systems is not very effective.

This paper proposes an Adaptive Signal Iterative Projection and Interference Suppression (ASIPIS) algorithm, utilizing the characteristics of PFM interference signals and LEO constellation signals. The algorithm concentrates the energy of PFM interference, which is spread over a wide bandwidth, into a few frequency points, thereby enhancing the interference's concentration and its separation from the LEO satellite signals. This effectively reduces the overlap between the LEO satellite signals and interference. The algorithm then uses subspace projection to map the interference and desired signals into different projection subspaces, eliminating the interference components and minimizing the damage to the desired signal during the interference suppression process. Finally, simulations and experiment results validate the enhanced performance of the proposed algorithm. The results demonstrate that the method can effectively eliminate single/multiple-component PFM interference, causing minimal damage to SOP signals, and is applicable to high-precision positioning receivers.

2 LEO satellite signal and PFM interference signal model

In an interference environment, the signal model at the input of the LEO satellite downlink receiver can be represented as:

$$x(t) = \sum_{i}^{N} s_i(t) + \sum_{m}^{M} j_m(t) + n(t) \tag{1}$$

Where $s_i(t)$ represents the signal received from the i-th LEO satellite (i = 1,2,3,…N), N represents the number of LEO satellites visible during the signal reception period, and $j_m(t)$ represents the interference signal of the mth component received by the receiver (m = 1,2,3,…,M). M represents the number of interferences received, and n(t) denotes the Additive White Gaussian Noise (AWGN) with a mean of zero.

When considering the received signal of a single LEO satellite, the reception signal of the i-th satellite can be expressed as Equation 2 [40]:

$$s_i(t) = AD(t)\cos\left(\omega_0 t + \varphi\right) \tag{2}$$

Where A is the signal amplitude, D(t) is the data code level value broadcasted by the satellite, ω_0 is the signal broadcast frequency, and φ is the broadcast phase.

$j_m(t)$ is PFM interference, and its instantaneous frequency $f(t)$ varies periodically over time, represented as:

$$f(t) = f_{0m} + \Delta f_m \cdot \sin\left(\frac{2\pi t}{T_m}\right) \tag{3}$$

Where f_{0m} is the carrier frequency of the PFM interference signal, Δf_m is the modulation amplitude of its frequency, T_m is the modulation period (MP) of the interference, $\sin\left(\frac{2\pi t}{T_m}\right)$ is the periodic modulation function, and the instantaneous frequency $f(t)$ of the interference oscillates periodically within the range of $[f_{0m} - \Delta f_m, f_{0m} + \Delta f_m)$.

Then, the phase function $\phi(t)$ can be expressed by Equation 3 as Equation 4:

$$\begin{aligned}\phi(t) &= 2\pi\int_0^t f(\tau)d\tau = 2\pi\int_0^t \left(f_{0m} + \Delta f_m \cdot \sin\left(\frac{2\pi\tau}{T_m}\right)\right)d\tau \\ &= 2\pi f_{0m}t - \frac{\Delta f_m T_m}{2} \cdot \cos\left(\frac{2\pi t}{T_m}\right)\end{aligned} \tag{4}$$

So, the PFM interference signal $j_m(t)$ can be expressed as:

$$j_m(t) = A_m \exp\left[2\pi f_{0m}t - \frac{\Delta f_m T_m}{2} \cdot \cos\left(\frac{2\pi t}{T_m}\right) + \varphi_m\right] \tag{5}$$

Where A_m is the carrier amplitude of the PFM interference signal, φ_m represents the initial carrier phase of the PFM interference, which is a random variable uniformly distributed within the range of $[-\pi, +\pi)$. $2\pi f_{0m}t$ is the linear phase term of the interference, which determines the central frequency of the signal; $\frac{\Delta f_m T_m}{2} \cdot \cos\left(\frac{2\pi t}{T_m}\right)$ is the nonlinear phase term, representing the periodic variation of the frequency with time, with a period of T_m.

3 The adaptive signal iterative projection and interference suppression (ASIPIS) algorithm

This section proposes the ASIPIS algorithm based on the characteristics of PFM interference signals and LEO constellation signals. The algorithm eliminates the influence of LEO satellite signals in the input signal, isolates the PFM interference signal, and reconstructs the observation matrix by the modulation period of the interference. It concentrates the energy, originally spread over a wide bandwidth, into a single frequency point in the rearranged data, thereby enhancing the interference's concentration. Furthermore, a spatial projection method is used to construct the interference subspace and the noise subspace. Finally, the LEO satellite signals and PFM interference signals in the original observation matrix are mapped into the newly constructed subspaces to eliminate the interference components. This algorithm effectively overcomes the challenges that traditional anti-PFM interference algorithms based on single-antenna reception of LEO satellite signals cannot resolve.

3.1 Signal adaptive iterative cancellation

Due to the high signal-to-noise ratio (SNR) of LEO satellite signals on the ground (typically 15–30 dB), directly performing subspace decomposition would cause serious impacts and misjudgments in the division of the interference space. Therefore, before performing subspace decomposition, high-power LEO satellite signals need to be eliminated, and PFM interference should be isolated, to facilitate the subsequent division of the interference space. The ASIPIS algorithm eliminates the LEO satellite signals using the approach proposed in Ref. [35], which utilizes the SCCI algorithm. This method adaptively iterates to approximate and fit the power spectrum of the LEO satellite signals, thereby eliminating the impact of the LEO satellite signal power from the input signal.

Through analysis, it is found that the power spectrum of the input signal (signal and noise) in the LEO satellite signal reception scenario follows a chi-square distribution [41]. Based on this, a first-order expression for the relationship between the input signal power spectrum and the signal power spectral density is derived, and an approximation model is constructed.

$$Y_e(f) = aG_s(f) + b \tag{6}$$

Where $Y_e(f)$ is the estimated value of the input signal power spectrum, and $G_s(f)$ is the signal power spectrum.

Let the error between the input signal power spectrum $P(f)$ and the model estimate $Y_e(f)$ be Equation 7:

$$e(a,b) = \sum_{f=1}^{N} (aGs(f) + b - P(f)) \tag{7}$$

Where N is the number of FFT points, the mean square error (MSE) is Equation 8:

$$\begin{aligned} e(a,b)^2 = &\sum_{f=1}^{N} (aGs(f) + b - P(f))^2 = a^2 \sum_{f=1}^{N} Gs^2(f) + Nb^2 + 2ab\sum_{f=1}^{N} Gs(f) \\ &+ \sum_{f=1}^{N} P^2(f) - 2a\sum_{f=1}^{N} Gs(f)P(f) - 2b\sum_{f=1}^{N} P(f) \end{aligned} \tag{8}$$

Using the gradient descent method, the criterion of minimizing MSE between $P(f)$ and the model estimate $Y_e(f)$ is adopted. Through multiple rounds of adaptive iterations, in each iteration, the portion of interference higher than the model power spectrum estimate in that round is eliminated, thereby achieving the goal where the final estimated signal power spectrum in the iterative process is nearly identical to the true value. The parameter estimates a and b in Equation 6 are obtained, and then the input signal power spectrum mean $Y_e(f)$ is derived. The next step is to subtract the estimated power spectrum mean $Y_e(f)$ from the input signal power spectrum $P(f)$. This subtraction can be considered as removing the power spectrum value of the LEO satellite signal contained in the input signal, leaving approximately only the noise and PFM interference signals. At this point, the next step is to construct the interference subspace.

3.2 Construct subspace

After the previous step of adaptive iterative cancellation of the signal, the input signal approximately only contains noise and PFM interference signals, which can be derived from Equation 1:

$$\hat{x}(t) \doteq \sum_{m}^{M} j_m(t) + n(t) \tag{9}$$

For the multi-component PFM interference in Equation 9, let the periods of the m PFM interference signals be $T_1, T_2, \ldots, T_m$, then their least common multiple is T_M, that is Equation 10:

$$T_M = n_1 T_1 = n_2 T_2 = \cdots n_m T_m \tag{10}$$

Where $n_1, n_2, \ldots, n_m$ are positive integer.

Using nT_M (n as a positive integer) as the interval to truncate the input signal data in Equation 9, forming the observation data matrix:

$$\begin{aligned} \hat{X} &= \begin{bmatrix} \hat{x}(1) & \hat{x}(2) & \cdots & \hat{x}(c) & \cdots & \hat{x}(nT_M) \\ \hat{x}(nT_M+1) & \hat{x}(nT_M+2) & \cdots & \hat{x}(nT_M+c) & \cdots & \hat{x}(2nT_M) \\ \vdots & \vdots & \ddots & \vdots & \ddots & \vdots \\ \hat{x}((R-1)nT_M+1) & \hat{x}((R-1)nT_M+2) & \cdots & \hat{x}((R-1)nT_M+c) & \cdots & \hat{x}(RnT_M) \end{bmatrix} \\ &= \begin{bmatrix} \hat{x}_{1,1} & \hat{x}_{1,2} & \cdots & \hat{x}_{1,c} & \cdots & \hat{x}_{1,nT_M} \\ \hat{x}_{2,1} & \hat{x}_{2,2} & \cdots & \hat{x}_{2,c} & \cdots & \hat{x}_{2,nT_M} \\ \vdots & \vdots & \ddots & \vdots & \ddots & \vdots \\ \hat{x}_{R,1} & \hat{x}_{R,2} & \cdots & \hat{x}_{R,c} & \cdots & \hat{x}_{R,nT_M} \end{bmatrix} \\ &= \begin{bmatrix} \hat{x}_1 & \hat{x}_2 & \cdots & \hat{x}_c & \cdots & \hat{x}_{nT_M} \end{bmatrix} \end{aligned} \tag{11}$$

Where $R = \lfloor L_s / nT_M \rfloor$, $\lfloor \cdot \rfloor$ denotes the integer floor, L_s is the total length of the sampled data, $\hat{x}_c$ is a column vector, $\hat{x}_c = \begin{bmatrix} \hat{x}_{1,c} & \hat{x}_{2,c} & \cdots & \hat{x}_{R,c} \end{bmatrix}^T$, $\hat{x}_{r,c} = \hat{x}((r-1)nT_M + c) = j((r-1)nT_M + c) + n((r-1)nT_M + c)$, r represents the number of rows of the matrix, $r = 1, 2, \ldots, R$, and c represents the number of columns of the matrix, $c = 1, 2, \ldots, nT_M$. For PFM interference $j_m(t)$, from Equation 5, the expression at time $t + nT_M$ can be written as Equation 12:

$$\begin{aligned} j_m(t+nT_M) &= A_m \exp\left[2\pi f_{0m}(t+nT_M) - \frac{\Delta f_m T_M}{2} \cdot \cos\left(\frac{2\pi}{T_M}(t+nT_M)\right) + \varphi_m\right] \\ &= A_m \exp\left[2\pi f_{0m} t + 2\pi f_{0m} nT_M - \frac{\Delta f_m T_M}{2} \cdot \cos\left(\frac{2\pi}{T_M} t\right) + \varphi_m\right] \\ &= A_m \exp\left[2\pi f_{0m} t - \frac{\Delta f_m T_M}{2} \cdot \cos\left(\frac{2\pi}{T_M} t\right) + \varphi_m\right] \exp\left(2\pi f_{0m} nT_M\right) \\ &= j_m(t) \exp\left(2\pi f_{0m} nT_M\right) \end{aligned} \tag{12}$$

As can be seen from the above equation, when the time interval is nT_M, the PFM interference data differ only by a scaling factor. Therefore, the observation matrix of the PFM interference signal can be expressed as:

$$\begin{aligned} J &= \begin{bmatrix} j(1) & j(2) & \cdots & j(nT_M) \\ j(nT_M+1) & j(nT_M+2) & \cdots & j(2nT_M) \\ \vdots & \vdots & \ddots & \vdots \\ j((R-1)nT_M+1) & j((R-1)nT_M+2) & \cdots & j(RnT_M) \end{bmatrix} \\ &= \begin{bmatrix} j(1) & j(2) & \cdots & j(nT_M) \\ j(1)\exp(2\pi f_0 nT_M) & j(2)\exp(2\pi f_0 nT_M) & \cdots & j(nT_M)\exp(2\pi f_0 nT_M) \\ \vdots & \vdots & \ddots & \vdots \\ j(1)\exp(2\pi f_0 (R-1)nT_M) & j(2)\exp(2\pi f_0 (R-1)nT_M) & \cdots & j(nT_M)\exp(2\pi f_0 (R-1)nT_M) \end{bmatrix} \end{aligned} \tag{13}$$

From Equation 13, it can be seen that each element in the observation matrix is obtained by multiplying the corresponding element in the first row by a constant. Therefore, by multiplying each element of the first row by $-\exp\left(2\pi f_0 (r-1)nT_M\right)$ and adding it to the rth row, and performing elementary row transformations, the interference signal observation matrix in Equation 13 can be transformed into:

$$J = \begin{bmatrix} j(1) & j(2) & \cdots & j(c) & \cdots & j(nT_M) \\ 0 & 0 & \cdots & 0 & \cdots & 0 \\ \vdots & \vdots & \ddots & \vdots & \ddots & \vdots \\ 0 & 0 & \cdots & 0 & \cdots & 0 \end{bmatrix}_{R\times nT_M} = \left[j_1 \; j_2 \; \cdots \; j_c \; \cdots \; j_{nT_M} \right]_{1\times nT_M} \tag{14}$$

Where j_c is a column vector, represented as: $j_c = [j(c) \quad 0 \quad \cdots \quad 0]^T$

Through matrix calculations, the eigenvalue matrix of matrix $J \cdot J^H$ is obtained as Equation 15:

$$\Lambda = diag\left(j(1)\times\overline{j(1)} + j(2)\times\overline{j(2)} + \cdots + j(nT_M)\times\overline{j(nT_M)}, 0, \cdots, 0 \right) \tag{15}$$

The singular value matrix of matrix J is Equation 16:

$$\Sigma_J = diag\left(\sqrt{j(1)\times\overline{j(1)} + j(2)\times\overline{j(2)} + \cdots + j(nT_M)\times\overline{j(nT_M)}}, 0, \cdots, 0 \right) \tag{16}$$

That is, perform subspace decomposition on the data matrix truncated with a period of nT_M, and the interference is concentrated in the subspace corresponding to the first singular value.

Therefore, the periodic truncated data matrix $\hat{X}$ of Equation 11 can be subjected to subspace decomposition, that is:

$$\hat{X} = U\Sigma V^T = [U_1 \quad U_2 \quad \cdots] \begin{bmatrix} \lambda_1 & 0 & 0 \\ 0 & \lambda_2 & 0 \\ 0 & 0 & \ddots \end{bmatrix} \begin{bmatrix} V_1 \\ V_2 \\ \vdots \end{bmatrix} \tag{17}$$

Where $U = [U_1 \quad U_2 \quad \cdots]$ and $V = [V_1 \quad V_2 \quad \cdots]$ represent the left singular matrix and the right singular matrix, respectively, Σ represents the singular value matrix, and the subscript λ indicates the order of the main diagonal, with $\lambda_1 \ge \lambda_2 \ge \ldots \ge 0$.

From Equations 13, 14, it can be seen that the interference components in each column of the matrix have the same frequency, which corresponds to a single-frequency interference. According to Ref. [36], if the data in each column only differ in phase, the rank of the corresponding matrix is 1. If there is only PFM interference, the rank of matrix $\hat{X}$ is 1, i.e., $\lambda = 0$. In other words, by performing subspace decomposition on the data matrix formed by truncating with a period of nT_M, the PFM interference can be concentrated in the subspace corresponding to the first singular value. When there are other signal components (such as desired signals and noise) unrelated to the interference, the above conclusion still holds, and the desired signals and noise will be spread across the entire space, thus enabling the construction of the interference subspace.

Equation 17 can be rewritten as Equation 18:

$$\hat{X} = U\Sigma V^T = [U_j \quad U_n] \begin{bmatrix} \Sigma_j & 0 \\ 0 & \Sigma_n \end{bmatrix} \begin{bmatrix} V_j \\ V_n \end{bmatrix} \tag{18}$$

Where Σ_j corresponds to λ_1, Σ_n corresponds to $diag\{\lambda_2 \quad \lambda_3 \quad \cdots\}$, the right singular vector corresponding to Σ_j is V_j, $V_j = V_1$, and the corresponding left singular vector is U_j, $U_j = U_1$; Σ_n corresponds to the right singular vector V_n, $V_n = [V_2 \quad V_3 \quad \cdots]$, and the corresponding left singular vector is U_n, $U_n = [U_2 \quad U_3 \quad \cdots]$. The interference subspace P_{A_J} and noise subspace $P_{A_J}^{\perp}$ are constructed separately as follows by Equations 19, 20:

$$P_{A_J} = V_j {V_j}^T \tag{19}$$

$$P_{A_J}^{\perp} = V_n {V_n}^T \tag{20}$$

Truncate the original input signal data of Equation 1 (including LEO satellite signals) with nT_M as the interval, forming the observed data matrix X. Then, project X onto the subspaces constructed in the previous step as Equation 21.

$$U^{-1} X \left(V^{-1}\right)^T = X' \tag{21}$$

Extract the corresponding part Σ_n from the newly obtained data matrix X', i.e., remove the data corresponding to the first row and first column of matrix X' to obtain the data matrix X''. Multiply matrix X'' by the corresponding left and right singular vectors V_n and U_n, respectively, and then the data matrix with the interference components eliminated can be restored as Equation 22.

$$X_{after\_AJ} = U_n X'' {V_n}^T \tag{22}$$

Unfold the data in matrix X_{after_AJ} sequentially to obtain the interference-suppressed signal y(t).

3.3 Estimation of modulation period (MP)

The next step is to discuss the estimation of the PFM interference modulation period when forming the data matrix in the previous step. Since the interference and noise components in the received signal are statistically uncorrelated, their cross-correlation function theoretically approaches zero and can be ignored. Therefore, the following will estimate the period of the periodic component in the received signal through autocorrelation processing.

From Equation 9, the autocorrelation function of $\hat{x}(t)$ can be expressed as:

$$R_x(\tau) = \sum_{m=1}^{M} R_{j_m}(\tau) + R_n(\tau) = R_j(\tau) + R_n(\tau) \tag{23}$$

Where $R_{j_m}(\tau)$ and $R_n(\tau)$ are the autocorrelation functions of $j_m(t)$ and $n(t)$, respectively. Then,

$$\begin{aligned} \left|R_j(\tau)\right| &= \left| \sum_{m=1}^{M} R_{j_m}(\tau) \right| \\ &= \left| \sum_{m=1}^{M} \frac{A_m^2}{2} \exp\left(2\pi f_{0m}\tau\right) \lim_{T\to\infty} \frac{1}{T} \int_{-T}^{T} \exp\left\{ \frac{\Delta f_m T_m}{2} \cos\left(\frac{2\pi}{T_m} t \right) - \frac{\Delta f_m T_m}{2} \cos\left[\frac{2\pi}{T_m} (t-\tau) \right] \right\} dt \right| \end{aligned} \tag{24}$$

From Equation 24, it can be seen that:

$$\left|R_j(\tau)\right| \le \sum_{m=1}^{M} \frac{A_m^2}{2} \tag{25}$$

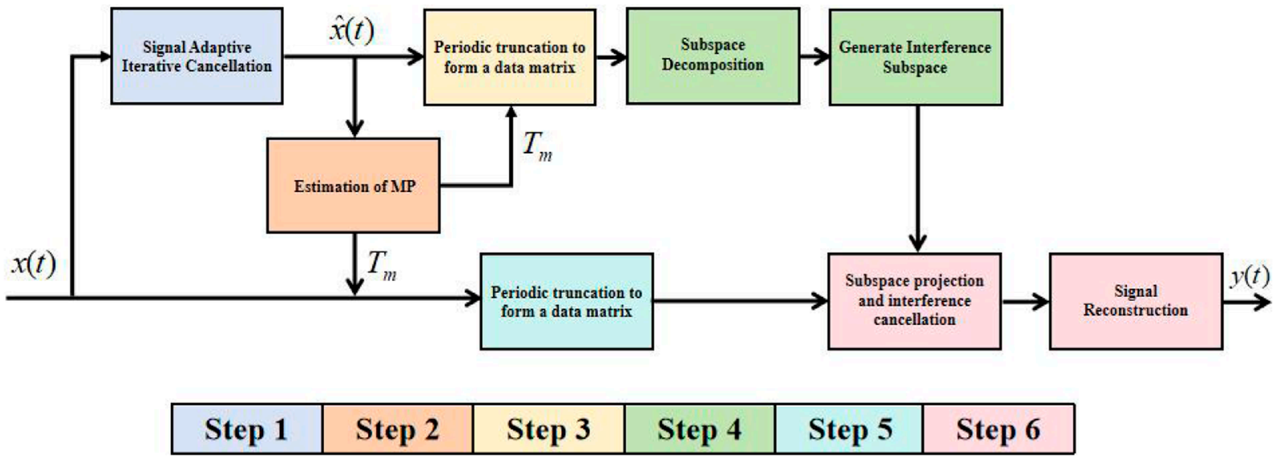

FIGURE 1
ASIPIS algorithm flowchart.

TABLE 1 Step of ASIPIS algorithm.

ASIPIS algorithm specific steps
Step 1: Start signal adaptive iterative cancellation on the original received signal to eliminate the power spectral value of LEO satellite signals, obtaining noise and interference signals
Step 2: Perform autocorrelation processing on the noise and interference signals obtained in the first step to obtain the modulation period estimate T_m
Step 3: Using the obtained modulation period to perform periodic truncation on the noise and interference mixed signal obtained in the first step, forming the observation matrix $\hat{X}$
Step 4: Perform subspace decomposition on the observation matrix $\hat{X}$ to construct the interference subspace
Step 5: Periodically truncate the original received signal using the modulation period to form the observation matrix X
Step 6: Project X onto the subspace constructed in Step 4, eliminate the interference components, and obtain the interference-suppressed signal

$\frac{\Delta f_m T_m}{2} \cdot \cos\left(\frac{2\pi t}{T_m}\right)$ is a periodic function with T_m as its modulation period, so Equation 25 holds true if and only if $t = nT_m$. That is, $|R_j(\tau)|$ reaches a maximum at nT_m. Therefore, by detecting the peaks of $|R_x(\tau)|$, the estimated value of the PFM interference modulation period T_m can be obtained.

At this point, the ASIPIS algorithm process can be summarized as shown in Figure 1:

The specific steps of the ASIPIS algorithm can be summarized as shown in Table 1.

4 Simulation and test verification

To verify the effectiveness of the proposed algorithm, relevant simulations and experiments were conducted. Without loss of generality, the Iridium system, a LEO constellation, was selected as the signal radiation source. The Iridium system consists of Polar-Earth-Orbit satellites at an altitude of 780 km, evenly distributed across six orbits in approximately the north-south direction. Each orbit contains 12 satellites (including one backup satellite), with an orbital inclination of 86.4° and an orbital period of 100.13 min, enabling global coverage. The user link adopts FDMA/TDMA/SDMA/TDD multiple access methods, grouping 12 adjacent beams from the 48-point beams of each satellite into a set for frequency reuse (SDMA) of the total available frequency band. Within each beam, the frequency band is divided into multiple TDMA channels by FDMA. In each TDMA channel, time division duplex (TDD) is applied for the uplink and downlink of the same user, meaning the uplink and downlink share the same TDMA carrier and frame but occupy different time slots. The total bandwidth allocated to Iridium is 1,616.0 MHz–1,626.5 MHz, with 1,616.0 MHz–1,626.0 MHz used for duplex channels as business channels, and 1,626.0 MHz–1,626.5 MHz used for downlink simplex channels as signaling channels [37, 38].

4.1 Simulation test

In the simulation experiment, the signal used was a downconverted Iridium intermediate frequency (IF) simulated signal with a center frequency of 270,833 Hz. The interference signal was set with a modulation type of Gaussian band-limited, having a mean of zero and a variance of one.

To validate the performance of the proposed algorithm, its anti-jamming capability was compared with other algorithms under different interference scenarios. In the interference scenario settings, multi-component PFM interference can be divided into two cases based on whether the carrier frequencies are consistent. The single-component PFM interference scenario can be considered a special case of multi-component PFM interference where the carrier frequencies are identical. Therefore, two interference scenarios were designed, with parameter settings as shown

TABLE 2 Interference scenarios parameter settings.

Interference scenario	Carrier frequency (kHz)	Modulation period (μs)	Bandwidth (kHZ)
Dual-component PFM interference scenario 1	270	360; 420	400; 250
Dual-component PFM interference scenario 2	270; 280	360; 420	400; 250

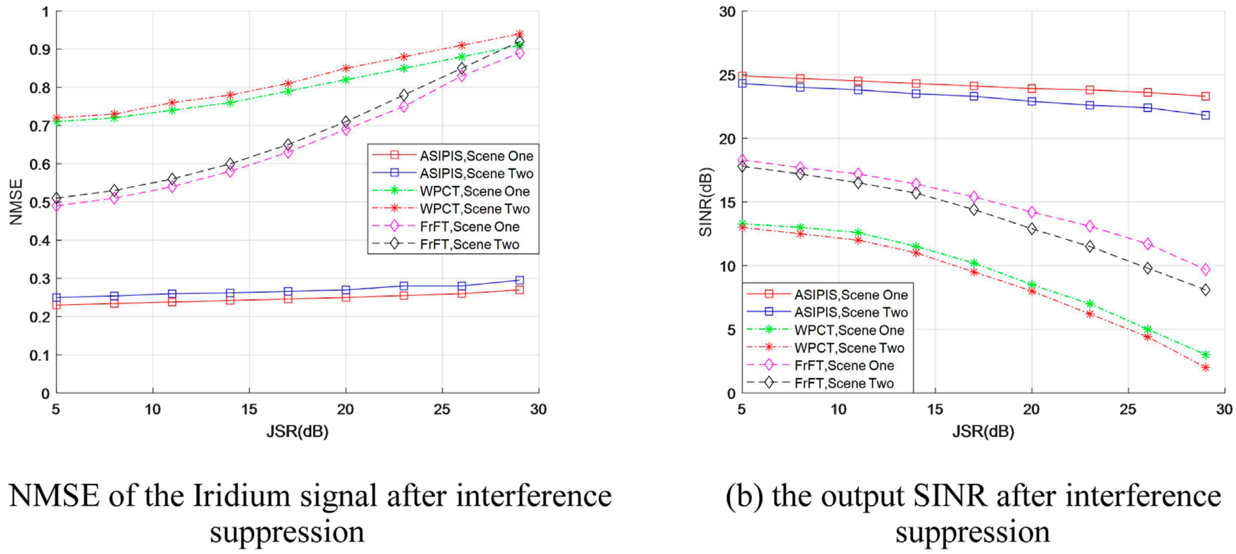

FIGURE 2
Verification of interference performance of various algorithms under interference scenarios. **(a)** NMSE of the Iridium signal after interference suppression. **(b)** the output SINR after interference suppression.

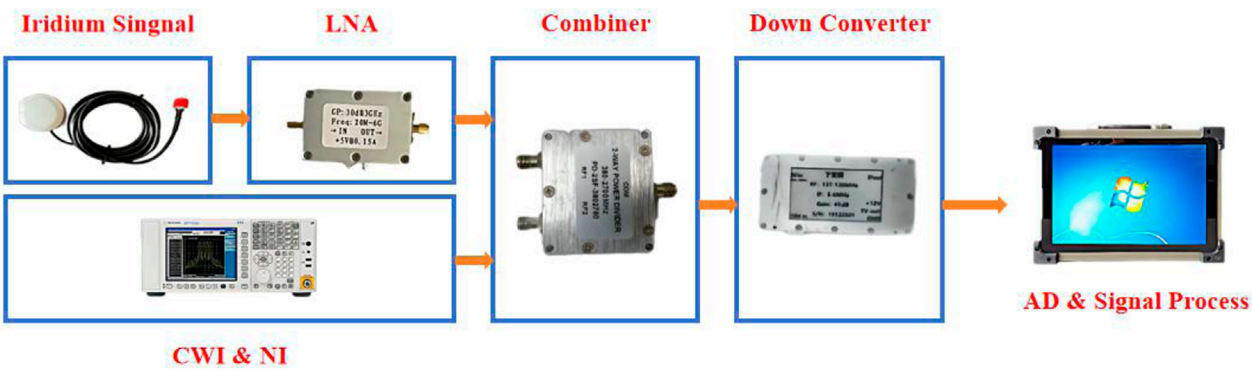

FIGURE 3
Hardware connection diagram.

in Table 2. The comparison algorithms include the Adaptive Wavelet Packet Coefficient Thresholding (WPCT) method [32] and the Time-Domain Combined Fractional Fourier Transform (FrFT) method [34]. For WPCT, the "Dmey" mother wavelet function was used, with five levels of wavelet decomposition, and soft thresholding was employed for interference detection and suppression. For FrFT, to search for the optimal order of the interference signal, the scanning points were set to 2000, and parameter estimation was performed only once for each batch of data.

When the input jamming-to-signal ratio (JSR) varies from 5 to 30 dB, Figures 2A, B respectively show the normalized mean square error (NMSE) of the Iridium signal after interference suppression processing and the output signal-to-interference-plus-noise ratio (SINR) under different interference scenarios, based on 50 Monte Carlo experiments.

(c) Experimental test scenarios

(b) Constellation map during the satellite visibility period

FIGURE 4
Actual experimental scenario. **(a)** Experimental test scenario. **(b)** Constellation map during the satellite visibility period.

TABLE 3 Experiment scenarios parameter setting.

Interference scenario	Carrier frequency (MHz)	Modulation period (μs)	Bandwidth (kHZ)
Dual-component PFM interference scenario 1	1,626.25	360; 420	400; 250
Dual-component PFM interference scenario 2	1,626.25; 1,626.26	360; 420	400; 250

As shown in Figure 2, the ASIPIS algorithm outperforms the other compared algorithms in terms of anti-jamming performance. Its output SINR and NMSE degrade only slightly as the input JSR increases, ensuring the successful acquisition of Iridium signals. The superior anti-jamming performance of the ASIPIS algorithm stems from its pre-subspace decomposition process, where high-power Iridium signals are removed to isolate PFM interference. This step eliminates the influence of Iridium signals on the interference detection process. Furthermore, the algorithm's performance is only marginally affected by increasing interference energy due to its periodic truncation and rearrangement method, which effectively concentrates the interference components into a single frequency. Subspace decomposition then projects the interference into a single subspace, achieving high interference concentration, reducing overlap between the desired signal and interference, and preventing the interference from spreading as its energy increases.

In contrast, the WPCT and FrFT algorithms show overall inferior anti-jamming performance. This is because, in the LEO satellite anti-jamming scenarios, the presence of high-power LEO signals significantly affects interference detection and suppression, leading to severe misjudgments. Traditional time-frequency-based interference suppression methods applied directly to these scenarios yield poor results. Their anti-jamming performance deteriorates rapidly with an increasing JSR due to the growing overlap between the desired signal and interference in the TF domain or FrFT domain as the number or energy of interference signals increases. This overlap results in damage to the desired signal during interference suppression, with more severe overlap causing greater signal loss. Specifically, the WPCT algorithm suffers from limited TF resolution, and higher interference energy leads to greater energy diffusion in the TF domain, negatively affecting the desired signal. While the FrFT algorithm improves the energy concentration of PFM interference to some extent, it is affected by spectral leakage inherent in digital FrFT implementations. Consequently, its interference suppression performance also degrades with increasing interference energy, though it remains superior to the WPCT algorithm.

4.2 Actual experimental verification

In the above simulation experiments, the ASIPIS algorithm's improved interference suppression performance has been verified. To further evaluate the effectiveness of proposed algorithm, a hardware platform was set up on the roof of the New Main Building at Beihang University, and real-signal anti-jamming experiments were conducted. The hardware platform is shown in Figure 3. This system uses a dedicated Iridium antenna to capture its signals. Gaussian interference signals generated by a signal source are combined with Iridium signals using a combiner. The combined signals are then frequency-shifted to IF through a down-converter. The system captures the signals at a sampling rate of 25 MHz, after which the signal reception and processing platform applies the anti-jamming algorithm for performance comparison. The experimental test scenario is shown in Figure 4A. During the test period, a total of four Iridium satellites were visible. The constellation map corresponding to the visible epoch of the Iridium satellites is shown in Figure 4B.

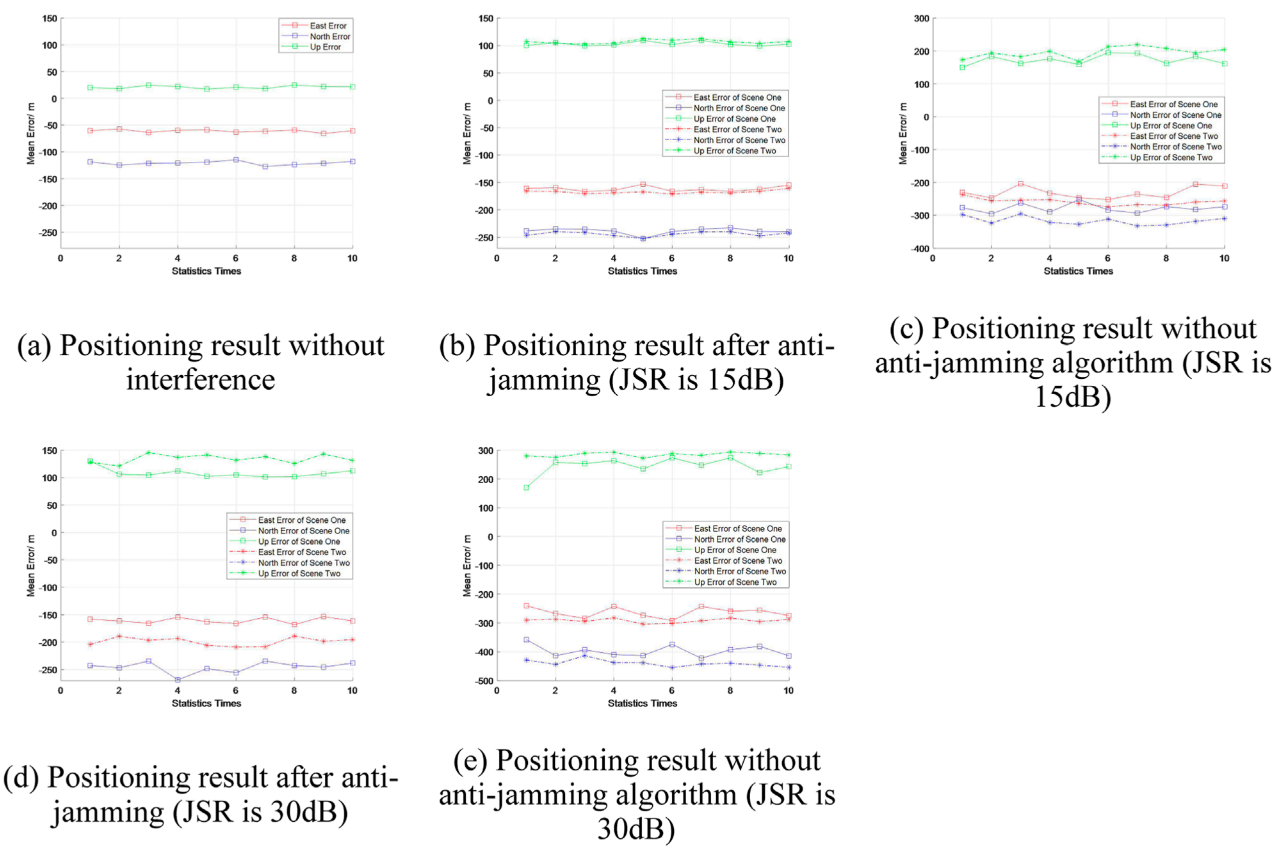

FIGURE 5
Comparison of positioning results in different scenarios. **(a)** Positioning result without interference. **(b)** Positioning result after anti-jamming (JSR is 15dB). **(c)** Positioning result without anti-jamming algorithm (JSR is 15dB). **(d)** Positioning result after anti-jamming (JSR is 30dB). **(e)** Positioning result without anti-jamming algorithm (JSR is 30dB)

Similarly, by configuring the signal source to generate interference scenarios of different intensities (with JSR of 15 dB and 30 dB, respectively), the ASIPIS algorithm was applied for anti-jamming processing. The positioning results after anti-jamming were compared with those obtained without activating the anti-jamming algorithm and under interference-free conditions. The interference scenario parameters are shown in Table 3.

The positioning results are statistically analyzed in the East-North-Up (ENU) coordinate system, comparing the positioning errors in the East-West, North-South, and Upward directions with the reference point coordinates. During the result analysis, the average of 50 positioning results is considered as one trial, and a total of 10 trials are conducted. The obtained results are shown in Figure 5.

The positioning results indicate that, compared to the positioning results under interference-free conditions, the positioning accuracy after interference suppression in interference scenarios shows a certain degree of decline. However, it still successfully retrieves Doppler information and achieves effective positioning. In contrast to interference scenarios where the interference suppression algorithm is not applied, activating the ASIPIS algorithm significantly improves positioning accuracy. The experimental results further validate the effectiveness of the ASIPIS algorithm and its interference suppression performance in LEO satellite PFM interference scenarios.

5 Conclusion

This paper proposes the ASIPIS algorithm, addressing the characteristics of narrow downlink bandwidth, high ground SNR in LEO constellation signals, and the generalized periodicity of PFM interference signals. The algorithm concentrates the dispersed PFM interference energy over a wide bandwidth into a few frequency points, enhancing the clustering of interference and its separation from LEO satellite signals. This effectively reduces the overlap between LEO satellite signals and interference. Additionally, subspace projection is employed to map the interference and desired signals into different subspaces, eliminating interference components and minimizing damage to the desired signal during anti-jamming processing. The algorithm comprehensively considers the effects of parameters such as PFM interference bandwidth, carrier frequency, modulation period, and intensity. Simulation and real data tests were conducted using Iridium signals from LEO systems for anti-jamming verification. Results show that, compared to traditional algorithms, this method effectively suppresses single/multi-component PFM interference, improving interference suppression performance under conditions such as narrow bandwidth and high power. It demonstrates significant enhancements in mitigating PFM interference in LEO satellite anti-jamming scenarios.

Data availability statement

The raw data supporting the conclusions of this article will be made available by the authors, without undue reservation.

Author contributions

LY: Writing – review and editing, Writing – original draft, Software. BF: Writing – review and editing, Supervision, Resources, Formal Analysis, Investigation, Funding acquisition, Methodology, Data curation, Project administration. HQ: Writing – review and editing, Writing – original draft, Methodology, Conceptualization. DX: Writing – review and editing. BG: Writing – review and editing, Supervision, Resources, Investigation. HS: Writing – review and editing, Methodology, Investigation, Conceptualization. GG: Writing – review and editing, Supervision, Investigation. ZL: Writing – review and editing, Supervision, Formal Analysis, Data curation. DH: Writing – review and editing, Visualization, Supervision, Software. LZ: Writing – review and editing, Supervision, Resources.

Funding

The author(s) declare that financial support was received for the research and/or publication of this article. This research was funded from the Army Academy of Artillery and Air Defense under Grant 220214003.

Acknowledgments

The authors would like to thank the editors and reviewers for their efforts to help the publication of this paper.

Conflict of interest

The authors declare that the research was conducted in the absence of any commercial or financial relationships that could be construed as a potential conflict of interest.

Generative AI statement

The author(s) declare that no Generative AI was used in the creation of this manuscript.

Publisher's note

All claims expressed in this article are solely those of the authors and do not necessarily represent those of their affiliated organizations, or those of the publisher, the editors and the reviewers. Any product that may be evaluated in this article, or claim that may be made by its manufacturer, is not guaranteed or endorsed by the publisher.

References

1. Jia Q, Zukun L, Baojun L, Jie S, Zhibin X, Zhi W A survey of GNSS interference monitoring technologies. *Front Phys* (2023) 11:11–2023. Sec. Interdisciplinary Physics. doi:10.3389/fphy.2023.1133316

2. Danning Z, Yu L. Effects of ionosphere dispersion on wideband GNSS signals. *Front Phys* (2023) 11:11–2023. Sec. Space Physics. doi:10.3389/fphy.2023.1103159

3. Shaojie N, Binbin R, Feiqiang C, Zukun L, Jie W, Pengcheng M, et al. GNSS spoofing suppression based on multi-satellite and multi-channel array processing. *Front Phys* (2022) 10:10–2022. Sec. Space Physics. doi:10.3389/fphy.2022.905918

4. Takeshi I, Motoyuki K, Yusaku O, Tatsuya F, Fumiaki T, Iwao U. GNSS-acoustic observations of seafloor crustal deformation using a wave glider. *Front Earth Sci.* (2021) 9–2021. doi:10.3389/feart.2021.600946

5. Ting Y, Nan C. A preliminary view of the CYGNSS soil moisture-vegetation activity linkage. *Front. For. Glob.* (2023) 6–2023. doi:10.3389/ffgc.2023.1320432

6. Binbin R, Feiqiang C, Shaojie N, Chunyang H, Zukun L, Shujian H. Performance analysis of repeater spoofing suppression based on GNSS multi-beam receiver. *Front Phys* (2022) 10:10–2022. Sec. Space Physics. doi:10.3389/fphy.2022.970132

7. Lei W, Lei C, Baiyu L, Zhe L, Zongnan L, Zukun L. Development status and challenges of anti-spoofing technology of GNSS/INS integrated navigation. *Front Phys* (2024) 12:12–2024. Sec. Space Physics. doi:10.3389/fphy.2024.1425084

8. Xiangjun L, Zukun L, Muzi Y, Wenxiang L, Feixue W, Yi Y, et al. Tradeoff of code estimation error rate and terminal gain in SCER attack. *IEEE Transactions Instrumentation Measurement* (2024) 73:1–12. doi:10.1109/tim.2024.3406807

9. Alexander M, Laurie B, Robert C, Walterio M, Jianing C, Colin G, et al. Visual odometry using pixel processor arrays for unmanned aerial systems in GPS denied environments. *Front. Robot.* 7–2020. doi:10.3389/frobt.2020.00126

10. Matteo F, Riccardo B, Matteo M On the precision of 6 DoF IMU-LiDAR based localization in GNSS-denied scenarios. *Front. Robot.* (2023). 10:2023. doi:10.3389/frobt.2023.1064930

11. Kassas ZM, Khalife J, Abdallah AA, Lee CI. I Am not afraid of the GPS jammer: resilient navigation via signals of opportunity in GPS-denied environments. *IEEE Aerosp Electron Syst Mag* (2022) 37:4–19. doi:10.1109/maes.2022.3154110

12. Zhang Y, Ho KC. Localization by signals of opportunity in the absence of transmitter position. *IEEE Trans Signal Process* (2022) 70:4602–17. doi:10.1109/tsp.2022.3198182

13. Hu Z, Li S, Xiang Y. Time information transmission based on FM broadcast signal. *IEEE Access* (2021) 9:16360–4. doi:10.1109/access.2021.3050410

14. Han K, Yu SM, Kim S-L, Ko S-W. Exploiting user mobility for WiFi rtt positioning: a geometric approach. *IEEE Internet Things J* (2021) 8:14589–606. doi:10.1109/jiot.2021.3070367

15. Zhao C, Qin H, Li Z. Doppler measurements from multiconstellations in opportunistic navigation. *IEEE Trans Instrum Meas* (2022) 71:1–9. doi:10.1109/tim.2022.3147315

16. Zhao C, Qin H, Wu N, Wang D. Analysis of baseline impact on differential Doppler positioning and performance improvement method for LEO opportunistic navigation. *IEEE Trans Instrum Meas* (2023) 72:1–10. doi:10.1109/tim.2023.3235456

17. Duran MAC, D'Amico AA, Dardari D, Rydström M, Sottile F, Ström EG, et al. Chapter 3—terrestrial network-based positioning and navigation. In: D Dardari, E Falletti, M Luise, editors. *Satellite and terrestrial radio positioning techniques*. Oxford, UK: Academic Press (2012). p. 75–153.

18. Tan Z, Qin H, Cong L, Zhao C. New method for positioning using IRIDIUM satellite signals of opportunity. *IEEE Access* (2019) 7:83412–23. doi:10.1109/access.2019.2924470

19. Neinavaie M, Khalife J, Kassas ZM. Acquisition, Doppler tracking, and positioning with starlink LEO satellites: first results. *IEEE Trans Aerosp Electron Syst* (2022) 58:2606–10. doi:10.1109/taes.2021.3127488

20. Morales J, Khalife J, Kassas ZM. Simultaneous tracking of Orbcomm LEO satellites and inertial navigation system aiding using Doppler measurements. In: *Proceedings of the 2019 IEEE 89th vehicular technology conference (VTC2019-Spring)*. Malaysia: Kuala Lumpur (2019). p. 1–6.

21. Khairallah N, Kassas ZM. Ephemeris closed-loop tracking of LEO satellites with pseudorange and Doppler measurements. In: *Proceedings of the 34th international*

technical meeting of the satellite division of the institute of navigation (ION GNSS+ 2021). St. Louis, MO, USA (2021). p. 2544–55.

22. Morales-Ferre R, Lohan ES, Falco G, Falletti E. GDOP-based analysis of suitability of LEO constellations for future satellite-based positioning. In: *Proceedings of the 2020 IEEE international conference on wireless for space and extreme environments (WiSEE)* (2020). p. 147–52. Vicenza, Italy.

23. Leng M, Razul SG, See CMS, Tay WP, Cheng C, Quitin F. Joint navigation and synchronization using SOOP in GPS-denied environments: algorithm and empirical study. In: *Proceedings of the 2015 sensor signal processing for defence (SSPD), Edinburgh, UK*. New York, NY, USA: IEEE (2015). p. 9–10. September 2015.

24. Parkinson BW, Spliker JJ. *Global positioning system: theory and application*. Cambrige, MA, USA: American Insitute of Aeronautics and Astronautics Inc. (1996).

25. Qin H, Zhang Y. Positioning technology based on starlink signal of opportunity. *J Navig Position* (2023) 11:67–73. doi:10.16547/j.cnki.10-1096.20230110

26. Mitch R, Dougherty R, Psiaki M, Powell S, et al. Signal characteristics of civil GPS Jammers. *Proc.24th ION GNSS* (2011) 1907–19. Portland, OR, USA.

27. Ryan M., Ryan D., Mark P, Steven D., Brady O., Jahshan B., et al. Signal characteristics of civil GPS Jammers. Proceedings of the 24th International Technical Meeting of the Satellite Division of the Institute of Navigation (ION GNSS 2011), Portland, OR, (2011), 1907–1919.

28. Dovis F. *GNSS interference threats and countermeasures*. Norwood,MA, USA: Artech House (2015).

29. Ioannides R, Pany T, Gibbons G. Known vulnerabilities of global navigation satellite systems, status, and potential mitigation techniques. *Proc IEEE* (2016) 104(6):1174–94. doi:10.1109/jproc.2016.2535898

30. Gao G, Sgammini M, Lu M, Kubo N. Protecting GNSS receivers from jamming and interference. *Proc IEEE* (2016) 104(6):1327–38. doi:10.1109/jproc.2016.2525938

31. Rezaei M, Mosavi M, Abedi M. New GPS anti-jamming system based on multiple short-time Fourier transform. *IET Radar,Sonar Navigat* (2016) 10(4):807–15. doi:10.1049/iet-rsn.2015.0417

32. Mosavi M, Pashaian M, Rezaei M, Mohammadi K. Jamming mitigation in global positioning system receivers using wavelet packet coefficients thresholding. *IET Signal Process* (2015) 9(5):457–64. doi:10.1049/iet-spr.2014.0280

33. Sun K, Jin T, Yang D. An improved time-frequency analysis method in interference detection for GNSS receivers. *Sensors* (2015) 15(4):9404–26. doi:10.3390/s150409404

34. Huang K, Tao R, Wu K, Wang Y. Study on interference suppression based on joint fractional Fourier domain and time domain. *Sci China Technol Sci* (2011) 54(10):2674–86. doi:10.1007/s11431-011-4533-7

35. Yao L, Qin H, Gu B, Shi G, Sha H, Wang M A study on anti-jamming algorithms in low-earth-orbit satellite signal-of-opportunity positioning systems for unmanned aerial vehicles. *Drones* (2024) 8(4):164. doi:10.3390/drones8040164

36. Kanjilal PP, Palit S. On multiple patternextraction using singular value decomposition. *IEEETransactions Signal Process.* (1995) 43(6):1536–40. doi:10.1109/78.388873

37. *Iridium burst detector and demodulator*. (2019) GNU Radio Iridium Out of Tree Module. Available online at: https://github.com/muccc/gr-iridium. Accessed July 4, 2023.

38. Iridium NEXT engineering statement. FCC File Number 1031348.

39. Mitch R, Dougherty R, Psiaki M., Powell S., OHanlon B., Bhatti J., et al. *Know your enemy: signal characteristics of civilGPS jammers[J]. GPS* (2012) 25:64–71.

40. Zhao C. *Research on fusion and differential positioning technology of iridium/orbcomm dual constellation signals of opportunity[D]*. Beihang University (2024).

41. Li J. *Strong interference supression for satellite navigation receiver with single antenna[D]*. National University of Defense Technology (2017).